ORIGINAL RESEARCH ARTICLE

$AlCoCrFeNiTi_{0.2}$ High-Entropy Alloy Under Plasma Nitriding: Complex Microstructure Transformation, Mechanical and Tribological Enhancement

MATEUSZ WŁOCZEWSKI, KINGA JASIEWICZ, PIOTR JENCZYK, ELŻBIETA GADALIŃSKA, KRZYSZTOF KULIKOWSKI, YONG ZHANG, RUI XUAN LI, and DARIUSZ M. JARZĄBEK

In this study, the $AlCoCrFeNiTi_{0.2}$ high-entropy alloy (HEA) was plasma nitrided to investigate the microstructure and mechanical properties of high-entropy nitrides formed in the surface layer of the bulk sample. XRD measurements revealed a BCC $\rightarrow$ FCC crystal structure transformation, with the σ phase disappearing and hexagonal aluminum nitride emerging. Further experimental studies on the nitrided samples, including SEM, EDS, and EBSD, uncovered element segregation into multiple FCC phases with similar lattice constants, such as the NaCl-type $(AlCrCoFeNiTi_{0.2})N$ high-entropy nitride. These observations align with theoretical analysis based on KKR-CPA calculations. Additionally, plasma nitriding induced high surface porosity; however, micropillar compression testing combined with nanoindentation revealed localized areas with significant hardness. A substantial reduction in the coefficient of friction was also observed. These findings not only provide deeper insights into the nitriding process of complex alloys, like dual-phase HEAs, but also hold promise for further exploration in the manufacturing of super-hard surfaces with high-entropy nitrides, enhancing mechanical properties for applications in harsh environments.

https://doi.org/10.1007/s11661-025-07752-1

I. INTRODUCTION

THE development of materials for both novel and conventional applications is being achieved by designing new materials, developing fabrication techniques, or combining both approaches. The latter is particularly valuable for extreme environments, such as nuclear power plants (NPP), engines, and industrial tools, where specific parts may require different properties at the surface than in the bulk. For example, a shaft in an NPP must possess high overall strength while offering low surface friction and wear resistance.

Using this approach, various materials and techniques have been developed. Currently, significant research is focused on high-entropy materials, such as high-entropy alloys (HEAs) and high-entropy ceramics (HECs).[1] Despite their exceptional bulk properties, surface modifications are often required to enhance their performance under specific conditions. Surface treatment of HEAs, for instance, can yield new and beneficial results, as these techniques enable the creation of hard or super-hard layers containing high-entropy ceramics (HEC)[2,3] on the surface of strong, ductile, radiation- and temperature-resistant materials.

Recently, high-entropy nitride coatings have garnered considerable research interest.[4–6] The most common fabrication method is reactive sputter deposition, primarily using magnetron sputtering with alloy targets and N_2 as the reactive gas.[5–7] However, this technique limits coating thickness to several microns due to residual stresses, and the coating's adhesion to the substrate may be inadequate for demanding applications. Plasma nitriding presents an interesting alternative for producing thicker and better-bonded nitride layers compared to reactive sputtering.[8,9] Plasma nitriding is particularly useful for materials containing strong oxide formers like aluminum, chromium, and titanium, which are challenging to nitride with conventional techniques.

MATEUSZ WŁOCZEWSKI and DARIUSZ M. JARZĄBEK are with the Institute of Fundamental Technological Research, 02-106 Warsaw, Poland and also with the Warsaw University of Technology, 00-661 Warsaw, Poland. Contact e-mail: djarz@ippt.pan.pl. KINGA JASIEWICZ and PIOTR JENCZYK are with the Institute of Fundamental Technological Research. ELŻBIETA GADALIŃSKA is with the Łukasiewicz Research Network – Institute of Aviation, Materials and Structures Research Center, 02-256 Warsaw, Poland. KRZYSZTOF KULIKOWSKI is with the Warsaw University of Technology. YONG ZHANG and RUI XUAN LI are with the Beijing Advanced Innovation Center of Materials Genome Engineering, State Key Laboratory for Advanced Metals and Materials, University of Science and Technology Beijing, 30 Xueyuan Road, Beijing 100083, P.R. China.
Manuscript submitted July 20, 2024; accepted March 13, 2025.

Published online: 03 April 2025

Notably, introducing nitrogen atoms into HEAs can intensify core effects[10]—namely, high mixing entropy, lattice distortion, sluggish diffusion, and the "cocktail effect"—which may influence both thermodynamic and mechanical properties. In cubic systems, nitrogen atoms, due to their small radius, may preferentially occupy interstitial positions, causing substantial lattice distortion and structural instability. This results in partially ordered high-entropy nitrides, where one sublattice is randomly occupied while the second is exclusively nitrogen.[11,12] Furthermore, the sluggish diffusion inherent to HEAs can hinder nitrogen migration into the bulk, accentuating differences between the surface layer and bulk properties.

Understanding the complex interplay between plasma nitriding and HEAs is a challenging yet promising field in materials science. Optimal selection of constituent elements is essential. For example, early transition metals from Groups IV and V (Ti, V, Zr, Nb, Hf, Ta) are strong nitride formers, while magnetic 3d elements with more valence electrons (Fe, Cr, Co, Ni) have a weaker affinity for nitrogen. Separate group forms p-elements (Al, Si, C), creating covalent bonding with N. This way, for nitriding, HEA can be tailored for best properties. However, it is unclear what combination of elements will be most suitable.[8,13–20]

Therefore, the main goals of this study are to elucidate the mechanisms underlying the plasma nitriding of HEAs and to explain the resulting changes in microstructure and surface properties. For this purpose, we plasma nitrided an $AlCoCrFeNiTi_{0.2}$ high-entropy alloy, which combines strong nitride formers (Ti), weak nitride formers (Co, Cr, Fe, Ni), and covalent bonding elements (Al). We then used nanoindentation and micropillar compression testing to examine changes in local mechanical properties (nano-hardness) and strength. FIB-milled cross-sections (including thin lamellae) and top surfaces were characterized via SEM, EDS, and AFM friction force measurements. The phase compositions before and after nitriding were determined by X-ray diffraction (XRD). Finally, theoretical analysis using the Korringa–Kohn–Rostoker method with a coherent potential approximation (KKR-CPA), which accounts for chemical disorder, was conducted to interpret the experimental microstructural findings.

II. EXPERIMENTAL

A. *Samples Preparation*

The bulk sample of $AlCoCrFeNiTi_{0.2}$ used in this study was the same as that from our previous publication,[21] prepared from high-purity elements (≥ 99.95 wt pct). Aluminum (Al), cobalt (Co), chromium (Cr), iron (Fe), nickel (Ni), and titanium (Ti) were combined in a ZG-2XF vacuum magnetic levitation-induction melting furnace. First, impurity gases in the furnace were evacuated to a pressure of 1×10^{-2} Pa, after which high-purity argon gas was introduced to approximately 400 Pa as a protective atmosphere. The raw materials were melted on a water-cooled copper hearth at approximately 1900 °C and levitated for 10 min for uniform mixing. The ingot was remelted and stirred three times to ensure homogeneity. During melting, the electromagnetic force from the coil levitated the molten materials, preventing contact with the crucible's inner walls. This separation minimized contamination and crystallization directionality, resulting in a high-quality alloy ingot.

The process yielded a 3 kg $AlCoCrFeNiTi_{0.2}$ alloy ingot (Φ100 × 120 mm), which was then cut into 5 mm × 5 mm × 3 mm pieces and polished. Polishing was done with grinding papers up to 2500 grit, followed by polishing with diamond particles down to 1/4 μm size. Final polishing was performed with a 60 nm SiO_2 suspension on a SAPHIR Vibro vibration-polishing device (ATM Qness GmbH, Germany) to minimize the thickness of the hardened surface layer. EBSD mapping confirmed the high-quality Kikuchi lines, indicating appropriate surface preparation. The glow nitriding process was conducted at 730 °C for four hours at a pressure of 2.2 mbar in an $N_2 + H_2$ atmosphere (2:1 ratio). Before nitriding, the samples were ultrasonically cleaned in acetone. The glow nitriding was performed using a high-temperature plasma treatment device. To prevent foreign material deposition from cathode sputtering, the plasma treatment chamber included structural elements, such as a cathode (sample table) and an anode (internal screen), both made of high-purity titanium (GRADE 2). The process temperature was monitored using a pyrometer calibrated to titanium emissivity and focused on the sample table.

B. *Microstructural Examination*

Thermodynamic simulations using ThermoCalc software were conducted to predict the nitriding temperature, phase structure, and its dependence on nitrogen concentration. For these calculations, the TCHEA6 database, specifically designed for HEAs, was utilized. Initially, phase diagrams for the base composition, $AlCoCrFeNiTi_{0.2}$, were generated. To examine how nitrogen concentration affects the alloy's microstructure, nitrogen levels were varied from 0 to 40 pct while maintaining the concentrations of other elements constant. These results allowed us to determine the optimal nitriding temperature.

X-ray diffraction (XRD) experiments were conducted to identify the crystalline phases present in the samples and their volume fractions. The measurements were performed using a MALVERN PANalytical Empyrean X-ray diffractometer with a copper X-ray tube, producing characteristic radiation at $\lambda_{K\alpha 1} = 1.540598$ Å. For the bulk sample, the diffraction experiment was performed with standard Bragg–Brentano geometry,[22] while for the specimen plasma nitrided, grazing incidence geometry. Polycapillary lenses of 70 mm length and 7 mm diameter focused the full X-ray power at a given point to create a quasi-parallel beam. A 0.02 mm nickel filter was used to remove the K_β component. The measurement area was restricted to 1×1 mm^2, and a 7.5 mm high anti-scatter slit with 0.04 rad Soller slits was included in the diffracted beam path. The

PIXcel1D-Medipix3 semiconductor detector recorded diffracted X-rays in continuous mode, covering an energy range from 4.02 keV to 16.1 keV, with measurements taken over 1219 points within the 2θ range of 30 to 100 deg and a step size of 0.0657 deg. Moreover, the incident angle for plasma nitride sample was constant (0.2 deg), which guaranteed small surface layer volume to be tested. Data analysis was performed using HighScore Plus 4.7a software and the ICDD-PDF5 + 2024 libraries.

Microstructural characterization was performed using a scanning electron microscope/focused ion beam (SEM/FIB) CrossBeam 350 (Zeiss, Germany). Morphology and topography were imaged using secondary electrons with 5 keV accelerating voltage and 30 μm aperture. Cross-sections and lamellae were prepared via FIB milling. To reduce milling artifacts and ion implantation, final polishing was performed with a 2 kV accelerating voltage and a 5 pA current. EDS mapping was conducted on cross-sections and lamellae, with 20 keV accelerating voltage and 120 μm aperture. FIB milling was also employed to prepare micropillars: for the untreated sample, nine pillars with diameters of 600 nm and nine with diameters of 1 μm were prepared, each with an aspect ratio of approximately 1. For the nitrided sample, the same initial sets of pillars were prepared, but due to variability in results, an additional set of nine 1 μm diameter pillars with an aspect ratio of 2 was also prepared. Milling was conducted in three stages with concentric rings of decreasing diameters and currents, with a final step using a 5 pA current and an inner diameter of either 600 nm or 1 μm. Each pillar's diameter and height were measured with SEM software to ensure precise values were used in subsequent calculations, especially critical for the nitrided sample where local microstructure variations affected milling rates.

C. *Mechanical Properties*

Nanoindentation was conducted using an in situ nanoindenter (Alemnis AG, Switzerland) equipped with a diamond Berkovich tip. Prior to measurements, the tip was calibrated on a fused silica sample. Three multi-cycle indentations were then performed at the center of both samples, with each indentation separated by at least 100 μm. Each test included 21 cycles of loading and unloading: eight cycles from 5 to 40 mN (in 5 mN increments), six cycles from 46 to 100 mN (in 10 mN increments), five cycles from 120 to 200 mN (in 20 mN increments), and two cycles from 250 to 300 mN (in 50 mN increments), as shown in Supplementary Information Figure S1. Each cycle began when the unloading force reached 0.5 mN, and the strain rate for all cycles was maintained at 0.1 s^{-1}. This approach generated hardness measurements for the same location at increasing depths. During post-processing, tip compression effects and any equipment drift were corrected using software provided by the manufacturer. Hardness and indentation depth were calculated with the Oliver-Pharr method,[23] ignoring the top 5 pct and bottom 30 pct of the unloading curve for model fitting.

Micropillar compression testing was conducted with the same in situ Alemnis nanoindenter, this time using a 5 μm diameter diamond flat punch. Compression was applied at a strain rate of 0.1 s^{-1}. Engineering stress versus engineering strain plots were generated using the exact dimensions of each prepared pillar, with $R_{0.2}$ (offset yield strength) and Rm (ultimate strength) determined. The results are discussed in detail due to significant curve shape variations observed in the nitrided sample. For certain pillars, strength values were not reported due to abnormal stress-strain curves.

Nanofriction force measurements were conducted using a FlexAFM (Nanosurf AG) atomic force microscope (AFM) equipped with a B2000-FM probe with a spherical, high-density DLC tip, 4 μm in diameter. Calibrations were performed prior to measurement for both normal and lateral forces. The normal-force calibration was conducted using the Sader method,[24] while lateral force calibration utilized a built-in device.[25] Friction tests were carried out under applied loads of 300 nN, 400 nN, 500 nN, and 600 nN, with a scan length of 10 μm and a scan speed of 3 s per line. Each test was repeated six times. Adhesion force between the tip and sample was determined using the standard AFM force-distance curve method.[26]

D. *Theoretical Calculation Details*

The electron structure calculations were performed using the full-potential KKR-CPA[27] technique implemented in the Munich SPR-KKR[28,29] package. The crystal potential was constructed using a local density approximation (LDA) framework with Vosko–Wilk–Nusair parameterization.[30] The angular momentum cutoff $l_{\max}$ was set to 3, which was sufficient for transition metals. Self-consistent cycles were repeated until convergence level of 10^{-5} Ry was achieved. The Fermi energy was calculated using the Lloyd formula.[28,31] The number of $\vec{k}$ points in the regular $\vec{k}$-point mesh was set to 48^3 (self-consistent cycles). The equilibrium lattice constants were calculated by fitting the E(V) function to the Birch-Murnaghan III order equation of state[32]:

$$E(V) = E_0 + \frac{9V_0B_0}{16}\left\{\left[\left(\frac{V}{V_0}\right)^{-\frac{2}{3}} - 1\right]^3 B\prime_0 + \left[\left(\frac{V}{V_0}\right)^{-\frac{2}{3}} - 1\right]^2\left[6-4\left(\frac{V}{V_0}\right)^{-\frac{2}{3}}\right]\right\} \quad [1]$$

For further analysis, it was convenient to replace the total energy with the formation energy, defined as the difference between E and the sum of the energies of the elements in their bulk form, according to their concentrations:

$$E_{\text{form}} = E_{\text{alloy}} - \sum c_i E_i \quad [2]$$

where c_i is the concentration of the ith element and E_i is the energy of the element in its bulk form.

The values of the equilibrium lattice constant a_0 (volume V_0), formation energy E_0, bulk modulus B, and

pressure derivative B_0 for all the considered systems are listed in the Supplemental Material (SI Table S1). To verify whether a particular nitride forms a specified crystal structure, theoretical XRD pattern were calculated (based on a_0) using VESTA software.[33]

III. RESULTS

A. *Microstructural Characterization*

In Figure 1(a), the results of the CALPHAD simulation performed with Thermo-Calc software indicate a possible complex structure of the nitrided HEA. The simulation suggests the formation of two disordered FCC A1 phases and simple aluminum nitride with a hexagonal, wurtzite structure. These phases are stable during nitriding, which is conducted at 730 °C (Figure 1(a)); therefore, this temperature was selected. Both DIS_FCC_A1#1 and DIS_FCC_A1#2 were modeled as consisting of two sublattices: (Al,Co,Cr,Fe,Ni,Ti)1 (N,N,VA)1, according to Thermo-Calc notation. Nitrogen concentration in DIS_FCC_A1#1 is 0 at pct, while in DIS_FCC_A1#2 it is 50 at pct. Additionally, a BCC phase can form upon cooling at temperatures below approximately 650 °C, and an FCC L12 phase can appear below 350 °C. Notably, the virgin sample consisted of two phases, sigma and BCC, as confirmed by the XRD results (Figure 2).[21] The exact elemental compositions of these phases, as determined by EDS, are shown in Table I.

On the other hand, the analysis of XRD pattern of the nitrided sample identified phases with dominating FCC and tetragonal structures (Figure 3). The analysis was performed using HighScore 4.7a software with ICDD PDF5 + 2024. It is important that the X-ray radiation beam does not reach the non-nitrided base material. No phases with body-centered cubic structures were observed, in contrast to the XRD pattern of the nitrogen-free sample. Additionally, the software identified the presence of chromium, titanium, and hexagonal aluminum nitrides.

Figure 4 presents SEM images of the virgin and nitrided samples. After careful polishing, the virgin sample surface becomes very smooth. The lighter and darker areas in Figure 4a correspond to grains with different crystallographic orientations. A closer look in Figure 4(b) shows that these grains exhibit a lamellar structure, comprising two phases: BCC and σ.[21] A similar lamellar pattern is also visible in the cross-section of the virgin sample (Figure 4(c)). In contrast, the nitrided material's surface layer loses these smooth features and becomes notably rough (Figure 4(d)). At higher magnification, the nitrided surface reveals craters and surface discontinuities (Figure 4(e)). These changes in the HEA's surface topography result primarily from the diffusion of nitrogen atoms during glow discharge, leading to lattice expansion and creating substantial stresses within the surface layer.[34,35] The cross-section of the nitrided sample displays a more complex structure than that of the virgin sample (Figure 4(f)), with significant disruption of the lamellar structure and the formation of pores.

In Figure 5 the SEM image and corresponding EDS maps of the surface of virgin sample are shown. The lamellae are composed of two different phases with different chemical compositions. The first phase was rich in nickel, aluminum, and titanium, and the second was rich in chromium and iron. On thew other hand, in

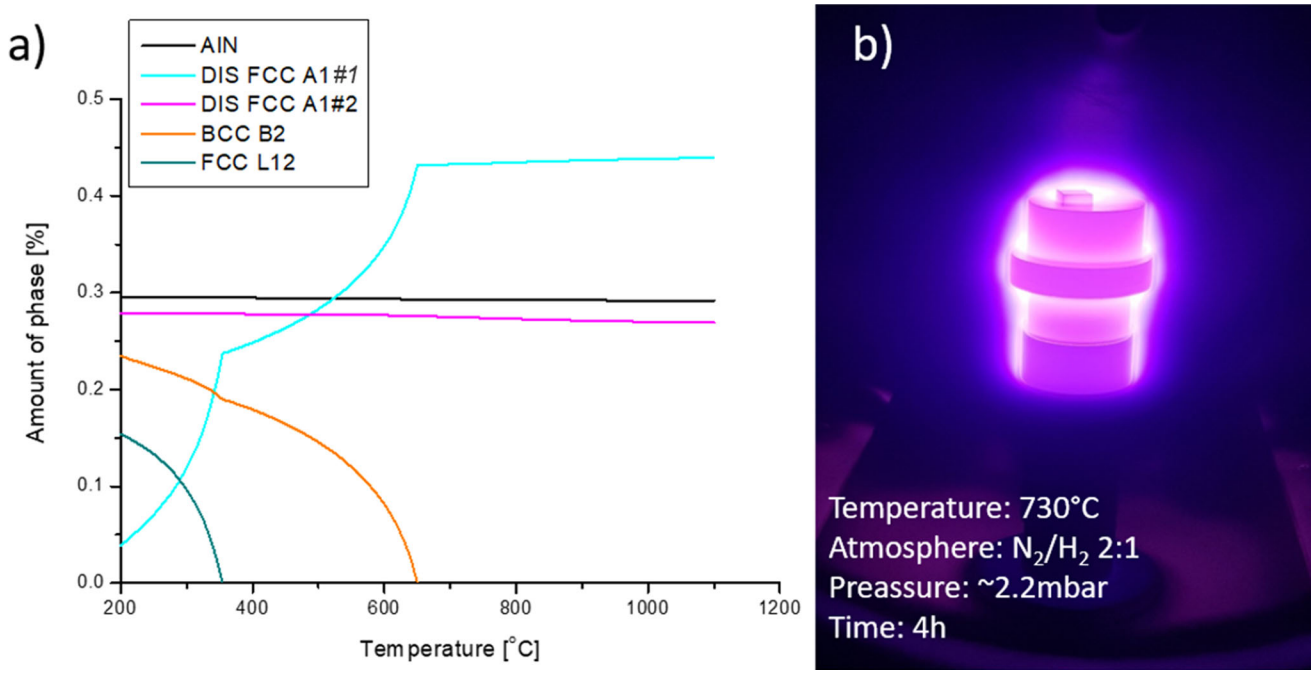

Fig. 1—Nitriding of HEA; (*a*) CALPHAD (ThermoCalc) predictions of the stable phases; (*b*) sample during nitriding.

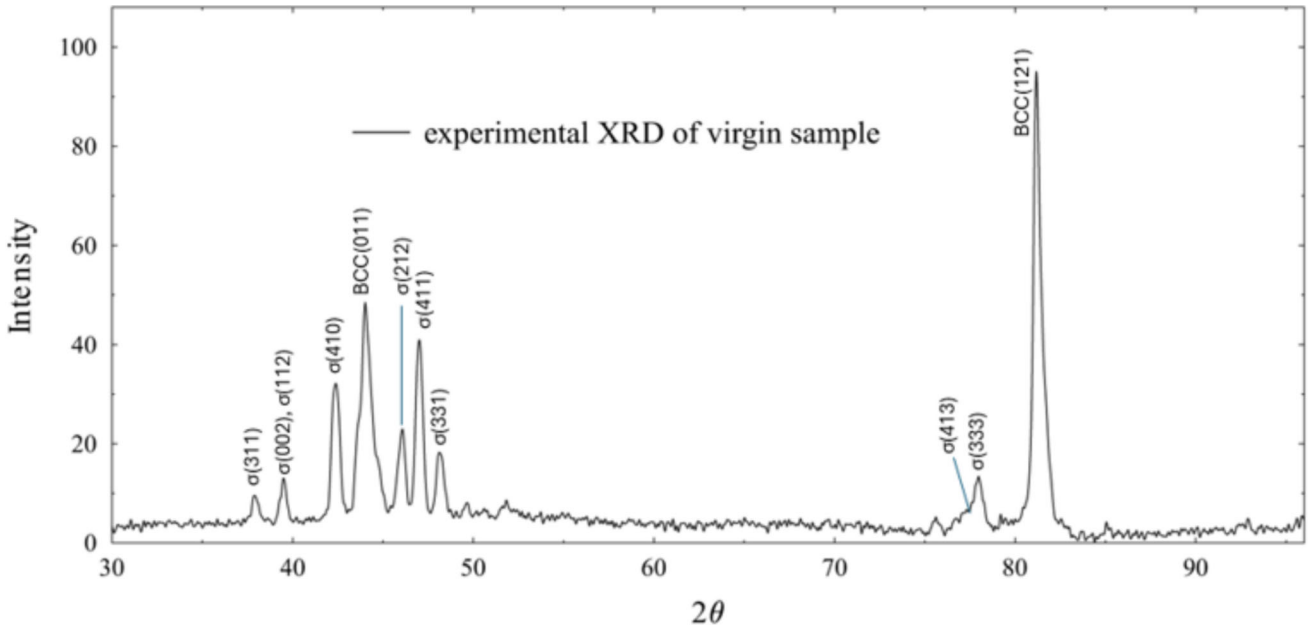

Fig. 2—X-ray diffractogram of virgin sample (BCC—body-centered cubic; σ—sigma phase).

Table I. Elemental Composition of the Virgin Sample

	Element	Al	Ti	Cr	Fe	Co	Ni
BCC Phase	at pct	22.9	4.3	14.7	17.2	20	20.9
Sigma Phase	at pct	5.6	1.3	34.3	28.5	19.1	11.3

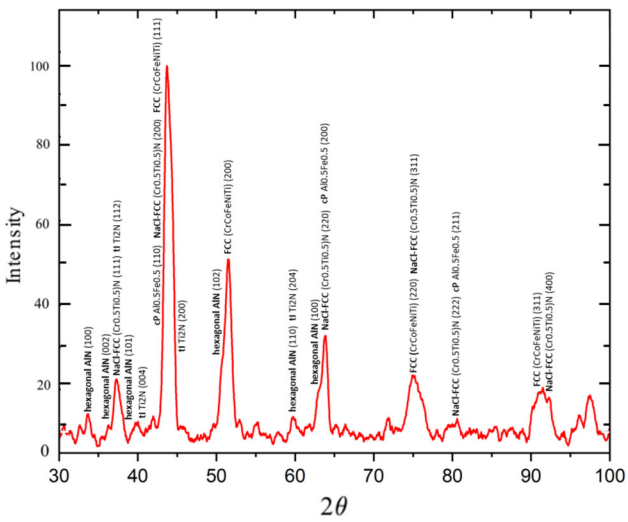

Fig. 3—X-ray diffractogram of nitrided sample (FCC—face centered cubic; tI—tetragonal, cP—CsCl primitive (B2) structure).

Figure 6 similar maps of the surfaces of the nitride samples are shown. Although segregation of the elements was also observed, it was significantly different from that in the virgin sample. There were areas richer in iron, nickel, and cobalt, and areas richer in titanium, chromium, and nitrogen. Finally, aluminum was distributed uniformly, but its concentration was significantly lower than that in the virgin sample, indicating that aluminum atoms diffused deeper into the sample. When larger areas were investigated, the elemental distributions were similar but not identical. The nitrogen distribution creates its own pattern. Nickel, aluminum, and cobalt were still distributed uniformly, but the spots were richer in these elements. Areas with significantly higher titanium content can also be clearly distinguished. Cr appeared at the highest concentration on the outskirts of these Ti-rich areas. The EDS maps at lower magnification are shown in the Supplementary Information (SI Figure S2).

To examine the in-depth structure and elemental distribution, particularly the diffusion of aluminum, a thin lamella (approximately 80 nm) was cut from a nitrided sample. The right side of Figure 7 shows the dark-field STEM image of this lamella, where crystalline or high-mass areas appear significantly brighter. Based on this contrast, it tentatively could be inferred that an amorphous layer or a highly dislocated nanocrystalline phase formed on the sample surface. Since XRD (Figure 3) did not show the presence of an amorphous phase, it was concluded that it was a highly dislocated nanocrystalline (CrCoFeNiTi)N. Beneath this layer lies a complex arrangement of crystalline phases. To verify this hypothesis and identify the crystalline phases, EBSD analysis was performed. Representative EBSD patterns are displayed on the right in Figure 7. These results do not completely agree with those of the X-Ray diffraction experiment. This was probably due to the specificity of the XRD and EBSD experiments. The diffraction experiment is by its nature a statistical experiment: in the case of the research for the subject of this article, the diffraction information was derived from a volume sampled at a depth of approximately 17 μm, and it should be noted that the proportion of the diffraction signal coming from the material layers

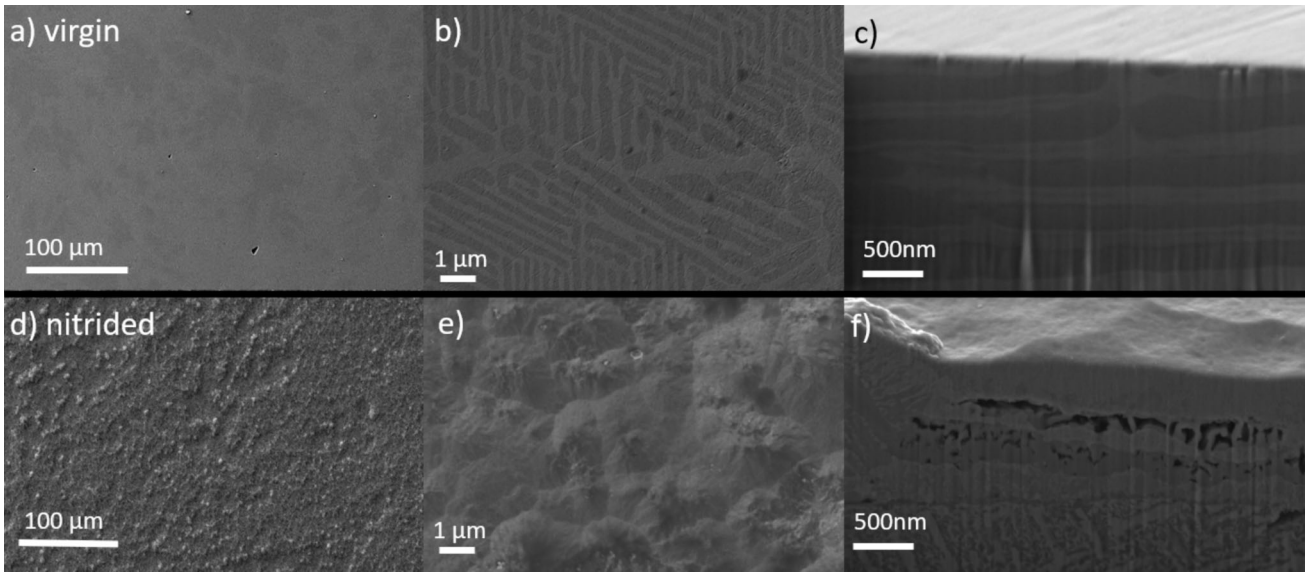

Fig. 4—SEM images of (top) virgin and (bottom) nitrided samples. (*a*), (*b*), (*d*), (*e*)—the samples surface. (c), (*f*) cross-sections.

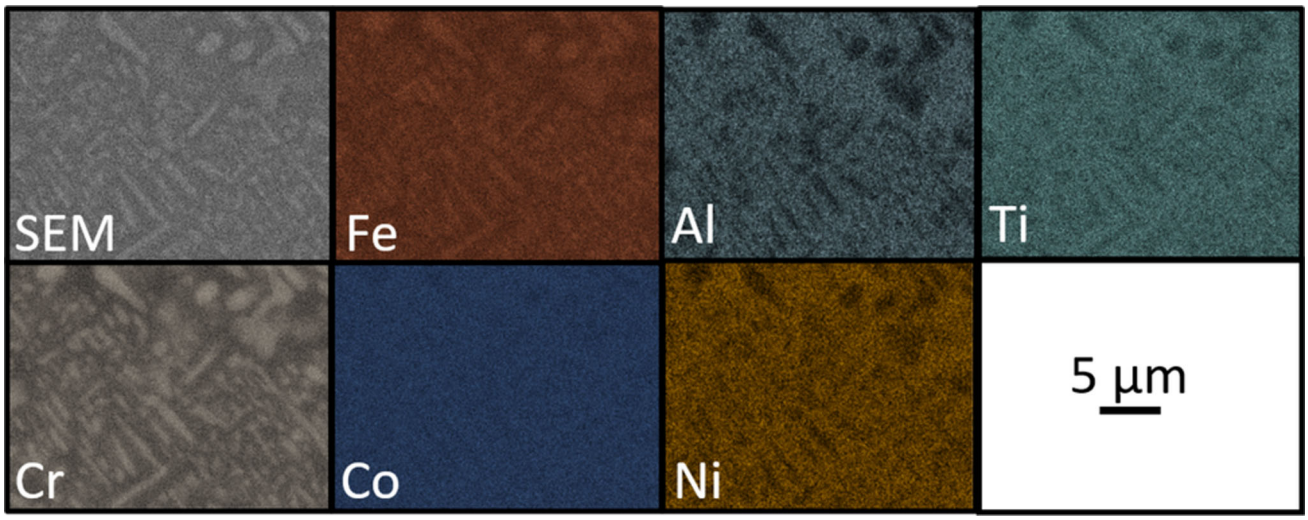

Fig. 5—EDS maps of the surface of virgin sample. The brighter phase on SEM, richer in chromium is the σ phase. The darker phase, richer in nickel is the BBC phase.

decreases exponentially with depth. In contrast, electron microscopy experiments such as EBSD are based on localized data from selected areas on the material surface. Hence, there may be discrepancies between the results of these experimental methods. Nevertheless, both experiments confirmed the presence of the dominant FCC phase.

EDS analysis was performed on the lamella, with the results shown in Figure 8. Exact values of elemental concentrations at various spots on the cross-section are provided in Supplementary Information Table S4. Nitrogen appears to be uniformly distributed to a depth of approximately 6–8 μm. Additionally, it is now evident that titanium migrates toward the sample surface, pushing aluminum deeper into the sample. Near the surface, titanium concentration is significantly higher than in other areas of the sample. The top layer also contains high concentrations of other elements, including nitrogen, iron, chromium, cobalt, and nickel. Just beneath this layer is a porous region rich in titanium, chromium, and nitrogen, indexed as an FCC structure but with a low confidence index, suggesting the formation of (Ti,Cr)N. According to Lee *et al.,* this nitride maintains an NaCl-type structure regardless of the Ti-to-Cr ratio.[36]

Deeper within the sample, brighter islands appear on the titanium map, indicating regions primarily containing titanium, chromium, and nitrogen. These correspond to areas where EBSD identified an FCC structure, with bright regions in the dark-field STEM image, signifying crystallinity and/or high atomic mass. Thus, these are also (Ti,Cr)N nitride precipitates, larger in size and producing clearer EBSD patterns. Conversely, hexagonal structures, containing primarily

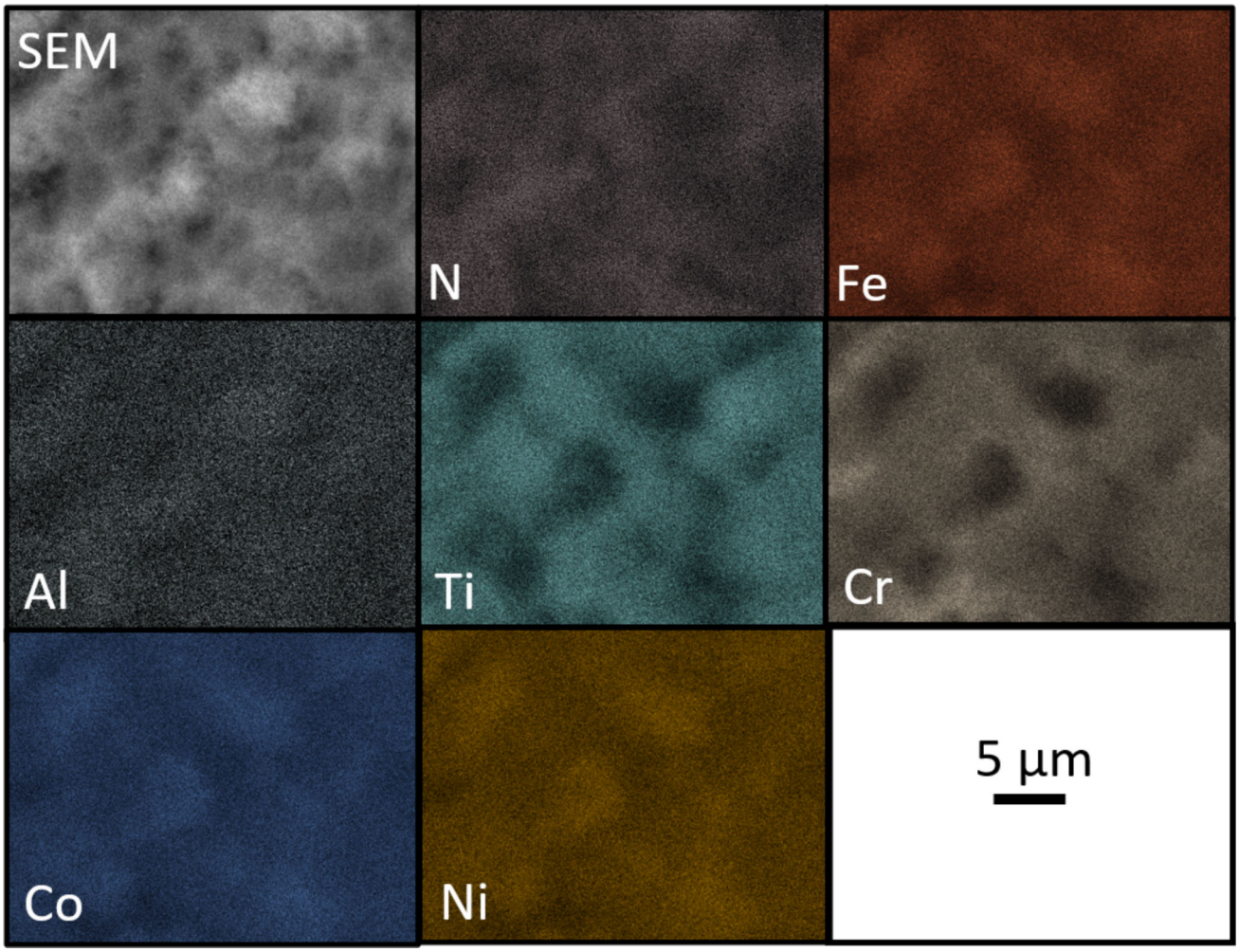

Fig. 6—EDS maps of the surface of the nitrided sample.

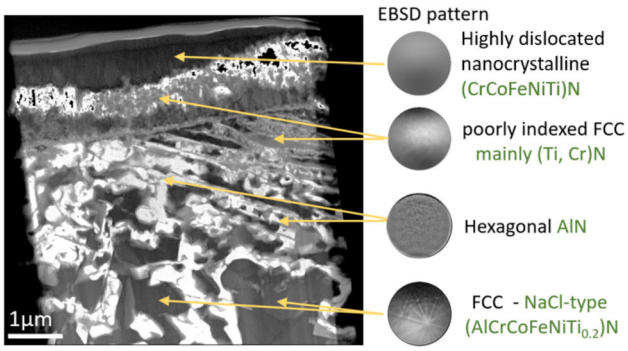

Fig. 7—Dark field STEM image of the lamella cut from the nitrided sample and EBSD patterns of different phases present in it.

aluminum and nitrogen, are likely aluminum nitrides. At the bottom of the lamella, darker regions in the STEM image show the presence of iron, cobalt, nickel, chromium, aluminum, and minimal nitrogen and titanium, with EBSD identifying them as FCC structures. These areas are attributed to an AlCoCrFeNi alloy, possibly with trace nitrogen interstitials.

To summarize the EDS and EBSD findings, Figure 7 uses green font to indicate the probable compositions of the identified phases.

B. *Mechanical Characterization (Indentation, Pillars, Friction)*

Multi-cycle indentation tests were conducted to investigate the mechanical properties of the samples. Figure 9 shows the hardness results and load-displacement curves. These tests revealed significant changes in hardness with depth for both samples. In the case of the virgin sample, the changes in hardness were influenced by the size effect for indentation depths less than 250 nm, where measurements were confined to small volumes of material, typically a single crystal. At depths greater than 250 nm, the interaction of a larger number of crystals and a more complex microstructure became evident, leading to a transition in hardness behavior.

In contrast, the hardness of the modified layer showed significant variation, which can be attributed to the complex structure of the nitrided layer. This structure includes porosity and various precipitates that appear at

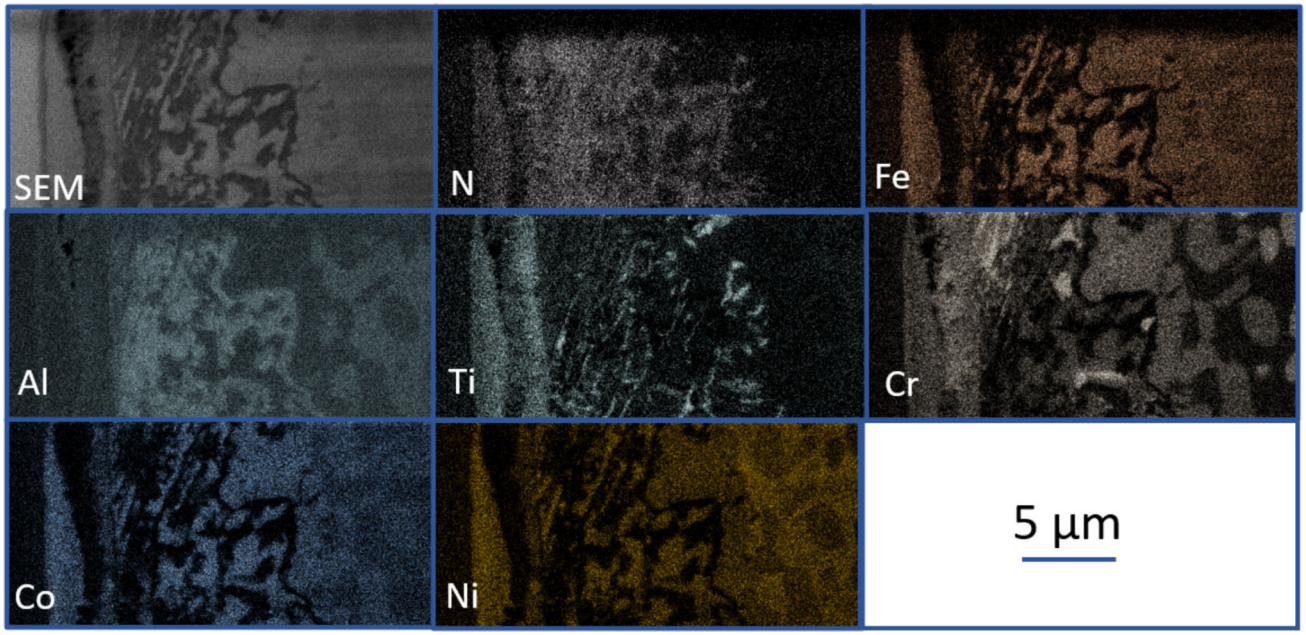

Fig. 8—EDS map of the lamella cut from the nitrided sample.

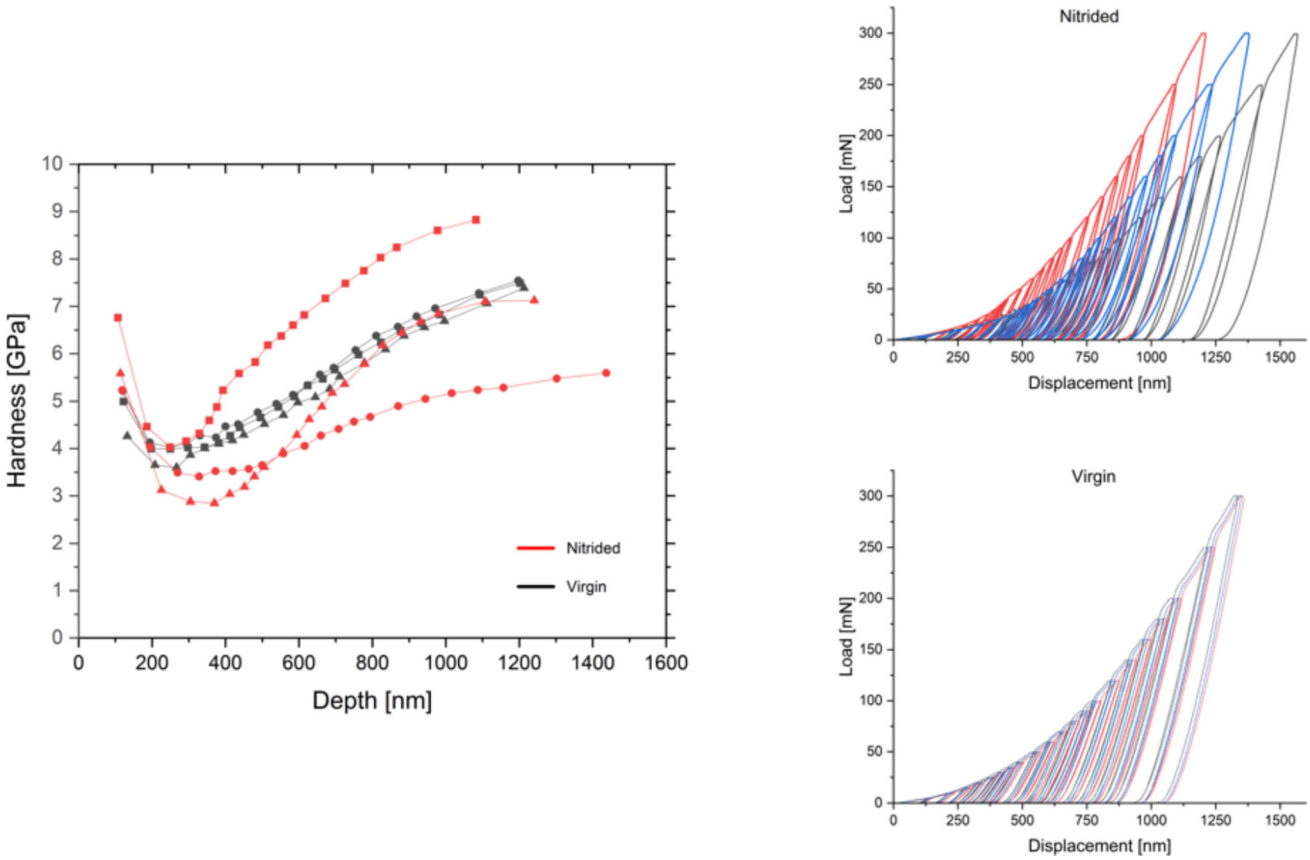

Fig. 9—Hardness results from the Oliver-Pharr method and corresponding multi-cycle indentation plots from nitride and virgin sample.

different depths. A notable increase in hardness was observed below 200 nm, likely due to the formation of a hard, nanocrystalline surface layer. As the indentation depth increased, the porosity caused a decrease in hardness, reaching a minimum between 250 and 400 nm. At greater depths, the presence of precipitates from different nitrides contributed to a considerable increase in hardness, reaching up to approximately 9

GPa. This is significantly higher than the maximum measured hardness of the virgin sample, which was approximately 7 GPa.

To further characterize the mechanical properties of the samples, micropillars were compressed using a suitable flat indenter to investigate the deformation mechanisms of the complex surface layer of the nitrided sample. This technique offers valuable insights into the behavior of individual layers, particularly the nitrided layers. It was observed that micropillars of different sizes (height and width) exhibited varying responses to loading. The engineering stress versus strain plots for the microcompression of each pillar type (with different sizes) are shown in Figure 10(b). The compression results, offset yield points ($R_{0.2}$), and compressive strength (R_m) are presented as column plots in Figure 10(a). Figures 11 and 12 show the corresponding SEM micrographs of the prepared and compressed pillars, respectively.

As previously mentioned, two types of pillars were fabricated: 600 nm and 1000 nm in diameter, with a height of approximately 1000 nm for both cases. Additionally, a series of larger pillars, approximately 1600 nm in height and 1000 nm in diameter, were created on the nitrided sample to account for the complex microstructure of the nitride layer and to investigate the deformation mechanism in deeper structures. These larger pillars are in Figure 12 denoted by "*."

Unfortunately, determining the offset yield point for the virgin samples with a 1000 nm diameter was not possible, as the pillars cracked at the grain boundaries before reaching the offset yield point (Figure 11(c)). The microcompression of non-nitrided samples with a 1000 nm diameter resulted in an R_m of 3.1 ± 1 GPa. In contrast, the $R_{0.2}$ of 600 nm diameter pillars was 2.3 ± 0.6 GPa for the virgin sample and 2.2 ± 0.9 GPa for the nitrided sample. For 1000 nm diameter pillars on the nitrided sample, $R_{0.2}$ was 2.6 ± 0.7 GPa. The $R_{0.2}$ of the larger pillars (1600 nm in height and 1000 nm in diameter) in the nitrided sample was much lower, at 1.0 ± 0.8 GPa.

The virgin samples were susceptible to brittle fracture along the grain boundaries, which was not related to the Portevin-Le Chatelier effect,[25] as observed in the compression plots with rapid stress peaks (Figure 10(b)) and in the SEM images of the compressed pillars (Figure 11(c)). On the other hand, the lower mechanical strength of the nitrided samples was attributed to significant porosity. However, as shown in the SEM images, there were areas of the nitrided sample that exhibited much higher strength compared to the reference material. In regions with lower porosity, the compressive strength increased, and the material near the surface deformed and eventually cracked. For instance, in Figure 12(d), the pillar's top layer is embedded in the porous layer underneath. As shown in Figure 12(e), the porous layer is fully compressed, while the top layer cracks. In the case of the highest pillars, sliding of the stronger layers (top and simple nitrides) along the areas of porosity was observed (Figure 12(f)).

Surprisingly, in contrast to the mechanical behavior, low scattering of the friction force was observed for the nitrided sample (Figure 13(a)). This can be explained by the fact that, during the friction measurement performed using AFM, the normal load was too low to involve the influence of the deeper layers on the resulting value. As a result, the measured friction force is primarily caused by the deformation of only the top layer—nanocrystalline high-entropy phase—with a relatively constant hardness, as well as the adhesion between this phase and the

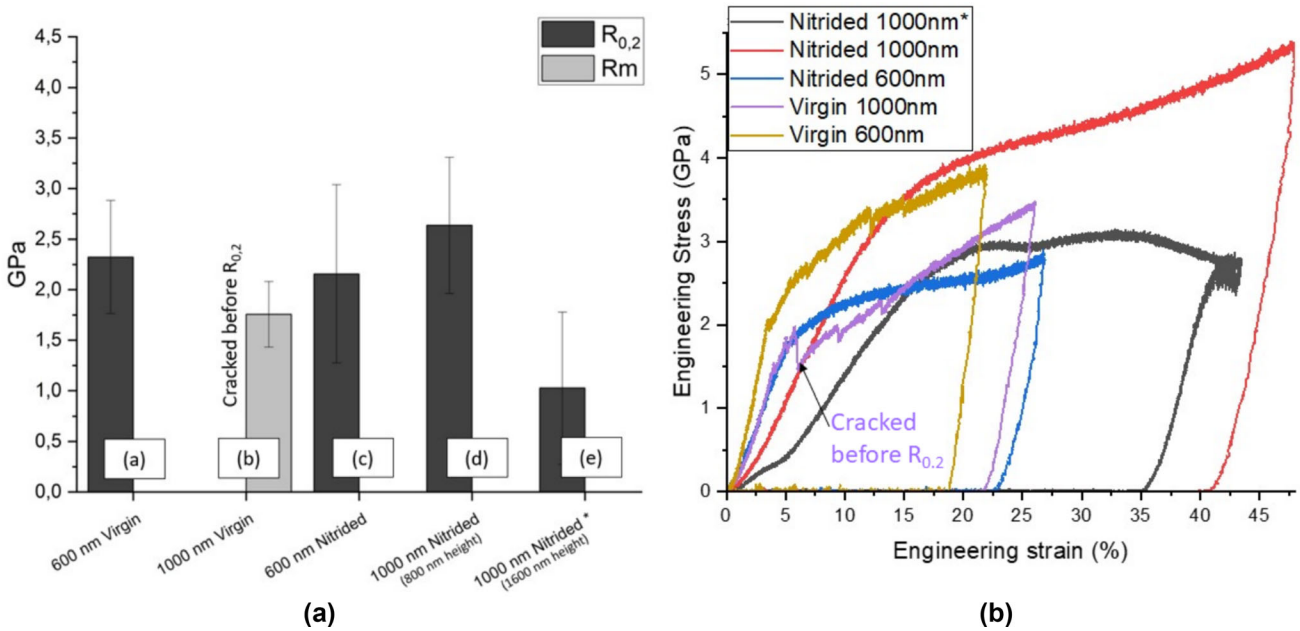

Fig. 10—Comparison of compression strength R_m and offset yield point $R_{0.2}$ from microcompression of pillars with different diameter (*a*) and engineering stress versus engineering strain plot (*b*).''*''—larger pillars, 1600 nm in height.

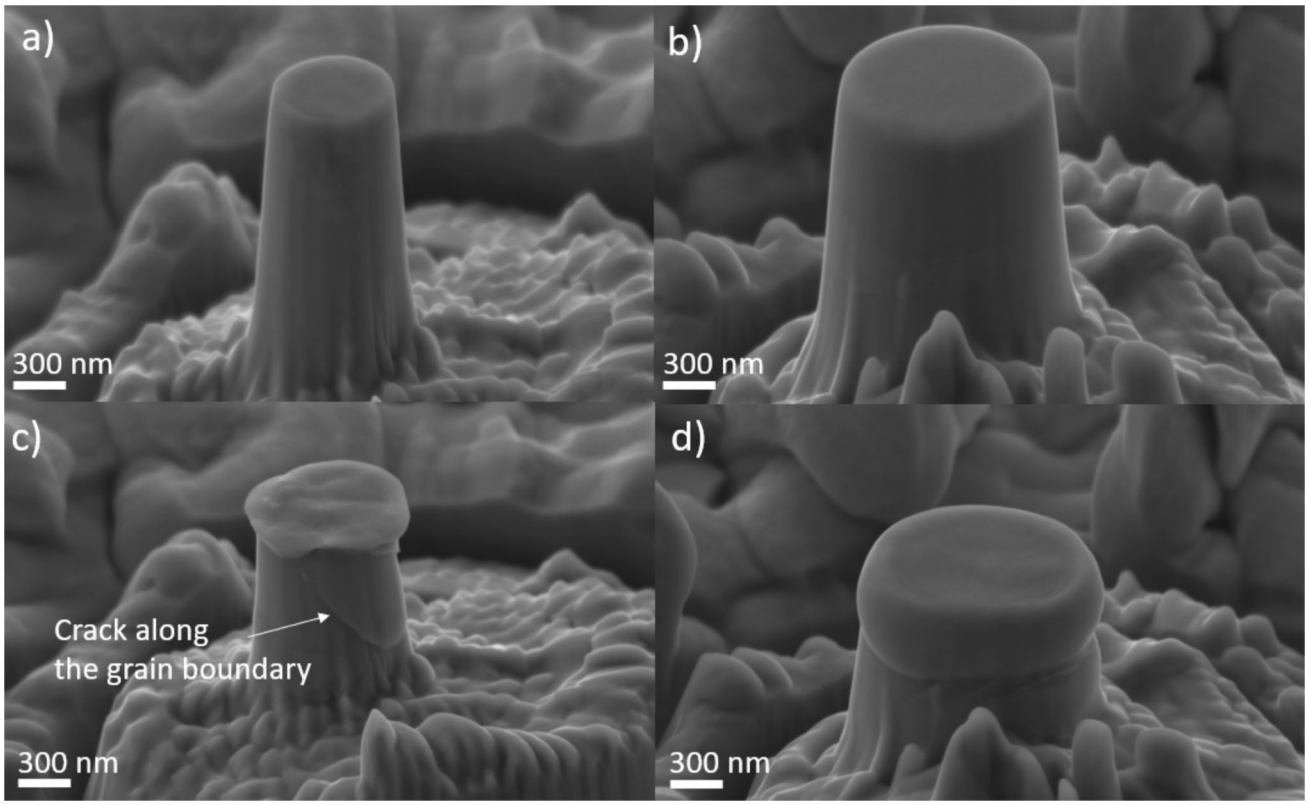

Fig. 11—Pillars with different diameter produced on the virgin sample before and after compression: (*a*) 600 nm before; (*b*) 1000 before; (*c*) 600 nm after; (*d*) 1000 nm after.

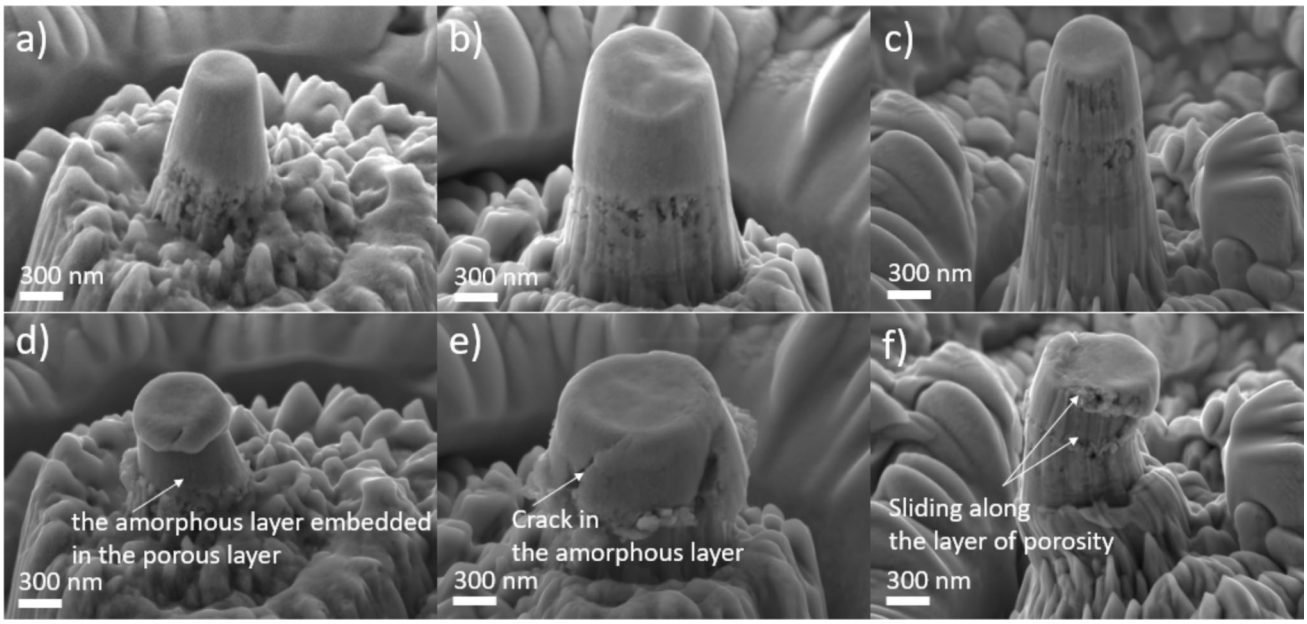

Fig. 12—Pillars with different diameter produced on the nitride sample before and after compression: (*a*) 600 nm before; (*b*) 1000 nm before; (*c*) 1000 nm* before; (*d*) 600 nm after; (*e*) 1000 nm after; (*f*) 1000 nm* after. ''*''—larger pillars, 1600 nm in height.

AFM tip. Notably, the friction force generally consists of two components: the deformation component, which depends on hardness, and the adhesion component.[21] For the virgin sample, the coefficient of friction (COF) generally reached very high values but decreased with higher loads. This suggests that the adhesion component becomes less significant as the load decreases.[37] A similar behavior can be observed for the nitrided

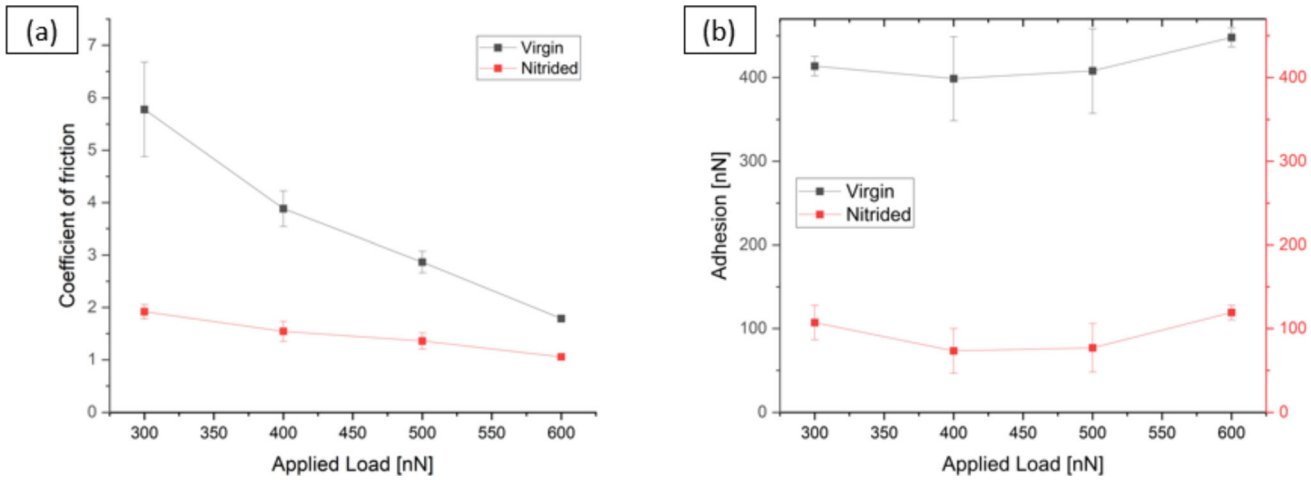

Fig. 13—Tribological interactions between a 4 μm diameter DLC ball and both virgin and nitrided samples under applied loads ranging from 300 to 600 nN. (*a*) Coefficient of friction and (*b*) adhesion. The lines connecting individual points serve as a 'guide for the eye.'.

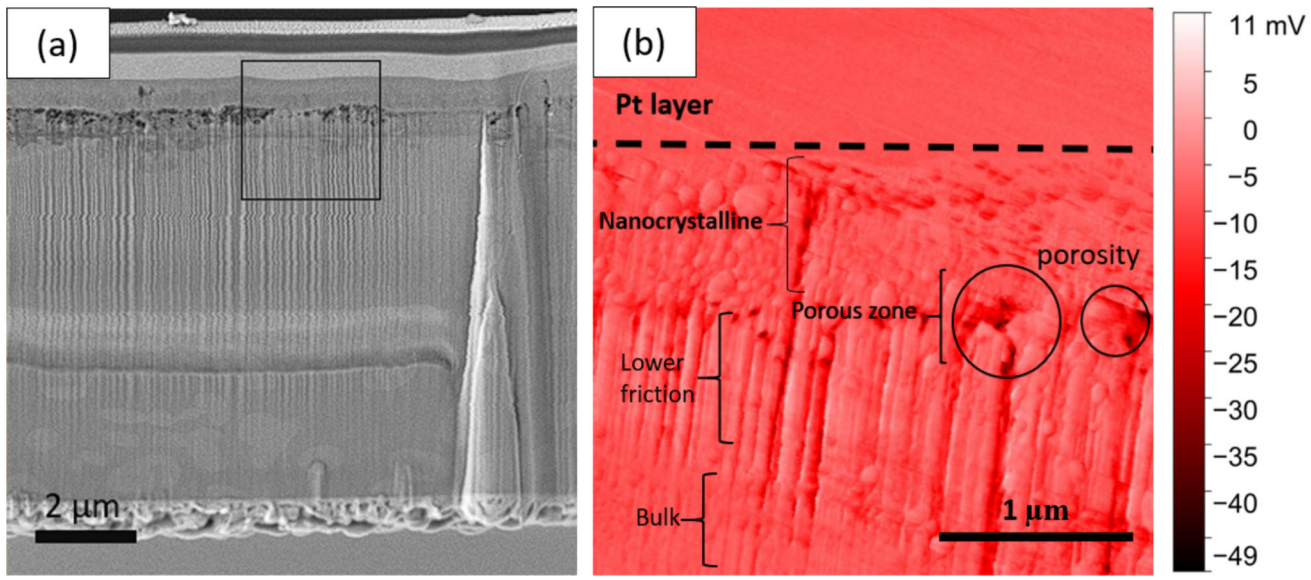

Fig. 14—Friction AFM signal on the cross-section of nitrided sample; (*a*) area indicated on SEM image; (*b*) AFM friction signal.

sample. However, due to its higher hardness and lower adhesion (Figure 13(b)), the COF was significantly lower for the nitrided sample. Notably, the adhesion (pull-off force) measured for the nitrided sample was approximately four times lower than that for the virgin sample. According to the AFM force-distance curves, it appears that in both cases, the adhesion does not depend on the applied load, at least within the range of the measurements.

Next, to gain an in-depth insight into the tribology of the nitrided layer, AFM friction tests were performed on the cross-section of the layer (Figure 14). The thin lamella of the cross-section was prepared using a Focused Ion Beam (FIB) and imaged with SEM (Figure 14(a)). The black border in the SEM image indicates the area investigated using AFM, as shown in Figure 14(b). A platinum (Pt) layer was deposited on top of the lamella during the preparation process. The AFM friction force measurements revealed three distinct zones in the material, each exhibiting different properties. The first zone is the dislocated nanocrystalline layer, which was not uniform. Clear areas with lower friction (brighter) and higher friction (darker) were observed in this region. Below this layer is a porous zone, followed by a zone containing multiple phases and compounds, primarily mixed FCC and hexagonal phases. This third zone exhibited significantly lower friction than the top nanocrystalline zone.

The dark lines seen in the AFM image represent artifacts created by the ion beam during the preparation process and should not be considered in the tribological analysis. Below the brighter zone, the bulk material was observed.

IV. DISCUSSION

In this section, we delve into the outcomes and implications of our experiments, aiming to unravel the intricate changes induced by plasma nitriding on the surface of an $AlCoCrFeNiTi_{0.2}$ high-entropy alloy. Firstly, the virgin sample of high-entropy $AlCoCrFeNiTi_{0.2}$ alloy is composed of two phases: BCC and σ. The content of the BCC phase is approximately 18 pct, with the remaining phase being σ. The intermetallic σ phase is known for its high brittleness,[38] especially in stainless steel,[39,40] as reflected in mechanical tests. Due to its high hardness, the σ phase in HEA[41] can serve as a strengthening phase, but when present in high concentrations, it leads to a very brittle material. In our study, the prepared micropillars from the virgin sample cracked within the elastic range, a result attributed to the high content of the brittle intermetallic σ phase.

In our previous study, we were able to induce a phase transformation and a high concentration of crystal structural defects by nitrogen ion implantation.[21] This treatment reduced the contribution of the σ phase, with both σ and BCC phases reaching approximately 50 pct each. Small amounts (up to 3.5 pct at the highest dose) of hexagonal forms of iron nitride and aluminum nitride also appeared. As the ion dose increased, the σ phase content continued to decrease, which resulted in improved mechanical properties, including hardness, wear resistance, and elastic recovery.

In contrast, in this work, the bulk sample was plasma nitrided with an applied voltage of 1 kV at 730 °C, and the microstructure obtained was significantly different. Both the σ and BCC phases transformed into FCC, hexagonal AlN, and an nanocrystalline structure.

To fully understand the complex microstructure obtained, we attempted to establish the phase composition of the nitrided sample using theoretical methods, specifically ab-initio calculations with the FP-KKR-CPA technique. Initially, we focused on the nitrogen-free $AlCrCoFeNiTi_{0.2}$ alloy (denoted as Al19.2Cr19.2Co19.2Fe19.2Ni19.2Ti4 in concentration notation). Two crystal structures were considered: BCC and FCC.

The panels in Figure 15(a) illustrate the relationships between formation energy and lattice constant, calculated for both the BCC (upper panel) and FCC (lower panel) phases. The values of a_0^{BCC} is 2.84 Å and a_0^{FCC} is are 3.58 Å. Both crystal structures exhibit similar interatomic distances at equilibrium, with 1.23 Å for BCC and 1.27 Å for FCC. The obtained formation energies are relatively low, on the order of mRy. From an energy perspective, the BCC phase is more stable, although the difference between E_{form}^{BCC} and E_{form}^{FCC} is not significant, amounting to only 1.8 mRy (24.5 meV). Repeating the calculations using the experimental composition of the BCC phase, measured by EDS (Al23Cr15Fe17Co20Ni21Ti4),[21] gave a slightly higher a_0^{BCC} of 2.85 Å. Using the equilibrium lattice parameters, theoretical XRD pattern (Figure 15(b)) were calculated and compared with the experimental diffractograms of the sample before (left panel) and after plasma nitriding (right panel). The analysis of the XRD results for the nitrogen-free HEA sample shows that it is composed of only BCC with $a = 2.88$ and σ phases, with a lattice constant of 2.88 Å for the BCC phase. The peaks in the theoretical XRD pattern of the BCC phase were almost identical to those in the experimental XRD pattern, although a minor discrepancy may arise from the local density approximation (LDA), which typically underestimates the lattice constant by 2 to 3 pct. Interestingly, such divergence in full-potential KKR-CPA appears only for BCC structures and is absent for systems crystallizing in FCC structures. According to Reference 42, the discrepancy in the lattice constants for BCC iron is 1.4 pct, whereas in the case of FCC nickel, the difference does not exceed 0.3 pct. These results support the above explanation of the observed differences between the theoretical and experimental XRD pattern of the nitrogen-free sample. The impact of the alloy composition should also be considered. In particular, the Al concentration strongly modified the lattice constant. This behavior was also observed for $Al_xCrCoFeNi$.[43] Theoretical equilibrium a_0 changes from 2.795 Å for Al concentration $c_{Al} = 10$ pct to 2.84 Å for $c_{Al} = 35$ pct. Titanium may also significantly affect the lattice constant because its atomic radius is higher than the radii of the other 3d elements. The total energy calculations for the hypothetical composition with slightly higher c_{Al} and c_{Ti}, that is $Al_{30}Cr_{15}Co_{15}Fe_{15}Ni_{15}Ti_{10}$, yielded a lattice constant of 2.87 Å

We did not observe the presence of the BCC phase in the plasma-nitrided samples. Recalculating the XRD pattern using a higher lattice constant yielded an even larger discrepancy from the experimental diffraction pattern.

Moving to the FCC phase, one can assume the presence of an insignificant error in the calculated a_0^{FCC} according to the results described above.[42]. The lattice constants should be approximately equal to the experimental values. Indeed, a good agreement between the theoretical XRD diffractograms of FCC structure with 3.58 Å and experimental diffractogram of nitrided sample have been achieved (Figure 15(b)). This phase might be a single FCC nitrogen-free high-entropy alloy with different elemental compositions; for example $Al_xCrCoFeNi$—the AlxCrCoFeNi-high-entropy alloy crystallized in the FCC structure when x is lower than ~ 0.6.[44]

In systems with cubic symmetry, nitrogen atoms, due to their small atom radius, may prefer filling interstitial positions rather than being incorporated into the crystal lattice and become a source of strong lattice distortion. Such high-entropy nitrides are partially ordered (one site with random occupation and the second sublattice occupied only by nitrogen atoms). Regarding the elements composing the investigated alloy, one should expect formation of high-entropy nitrides with NaCl- or ZnS-type crystal structures. In general, combination of nitrogen to transition metal atom in ratio 1:1 results in the formation of nitrides with NaCl-type (space group 225, Fm $\bar{3}$ m) or ZnS-type (space group 216, F $\bar{4}$ 3 m) FCC crystal structures, depending on which interstitial

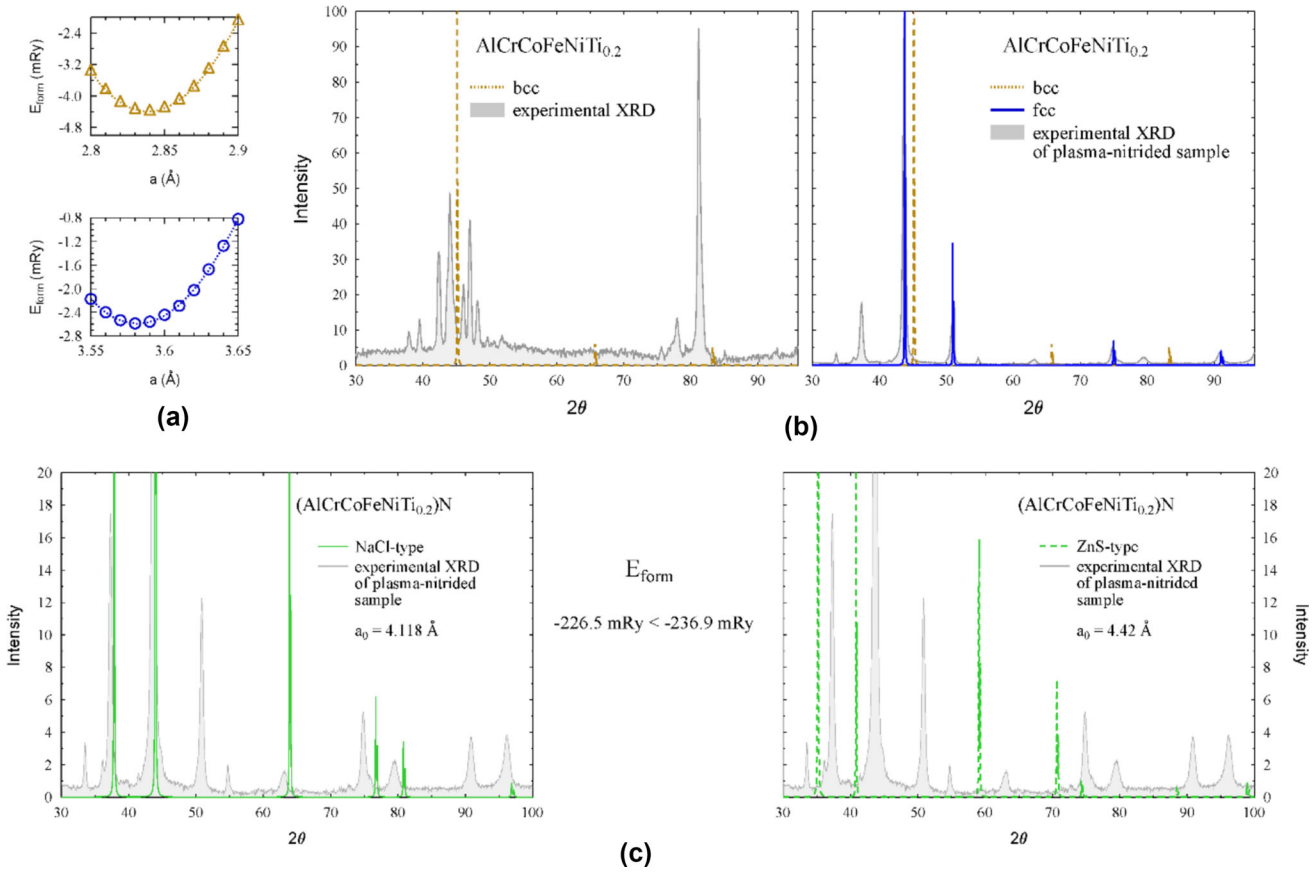

Fig. 15—Results of DFT simulations of the diffraction patterns. (*a*) relationships between formation energy and lattice constant calculated for BCC and FCC; (*b*) theoretical XRD pattern of $AlCrCoFeNiTi_{0.2}$ compared to the experimentally obtained ones; (*c*) theoretical XRD pattern of NaCl-type structure and ZnS-type structure of $(AlCrCoFeNiTi_{0.2})N$ compared to the experimental ones.

positions are occupied. In the first case, nitrogen prefers the octahedral positions 4a (0, 0, 0), whereas the ZnS type is formed when N atoms fill half of the available tetrahedral sites 4b ($\frac{1}{2}$,0,0).

As in the case of the nitrogen-free HEA, we started by computing $E_{form}(a)$ functions. Equilibrium lattice constant for rocksalt-type structure is 4.16 Å, while for zincblende-type structure value 4.42 Å have been obtained. The calculated XRD pattern (Figure 15(c)) of the NaCl-type structure are far more consistent with the experimental diffractogram of the nitrided sample than those of the ZnS-type structure. However, from an energy perspective, the zincblende-type structure is more stable, even though the difference in E_{form} is small at only 5 mRy (68 meV). A full analysis of the crystal stability requires lattice dynamics studies to check the appearance of soft-mode phonons, leading to structural instability. Vacancies on nitrogen sites also might have influence on formation energies, as well as taking spin polarization into account. Another possibility is the decomposition into binary and/or ternary 3d metal nitrides. However, there were still several peaks in the diffractogram that required explanation. More specifically, presence of NaCl-type and FCC structures do not explain peaks at $2\theta \sim 33$ deg and $2\theta \sim 55$ deg on experimental diffractogram of plasma-nitrided sample.

Considering AlN was helpful in establishing answers. Aluminum is a strong nitride former, but instead of an FCC structure, its nitride has a hexagonal, wurtzite-type structure with a two-atom basis: ($\frac{1}{3}$, $\frac{2}{3}$, u), where u of AlN is approximately 0.38. Despite the widely known lattice constants, we performed total energy calculations as a function of a and c/a ratios (right panel in Figure 16(a)). The motivation to calculate the theoretical lattice parameters was necessary to determine the level of divergence between FP-KKR-CPA and the experiments in the case of hexagonal systems. Calculated values for AlN are following: $a \approx 3.11$ Å and $c \approx 4.94$ Å (Figure 16(a)). Satisfactory reproduction of experimental data have been achieved according to the Reference 45 ($a = 3.112$ Å and $c = 4.98$ Å).

The localization of the peaks in the calculated XRD pattern of AlN confirms the assumption that aluminum nitride (AlN) was formed during the plasma nitriding of the HEA samples. Importantly, the formation energy of AlN was significantly lower than E_{form} of the nitrogen-free BCC and nitride NaCl-type/ZnS-type structures (Figure 16(a)).

The theory of structural transition provides an answer regarding the origin of the peak at $2\theta \approx 55$ deg. Because the $AlCrCoFeNiTi_{0.2}$ sample changes its structure after the plasma nitriding process from BCC to FCC, one

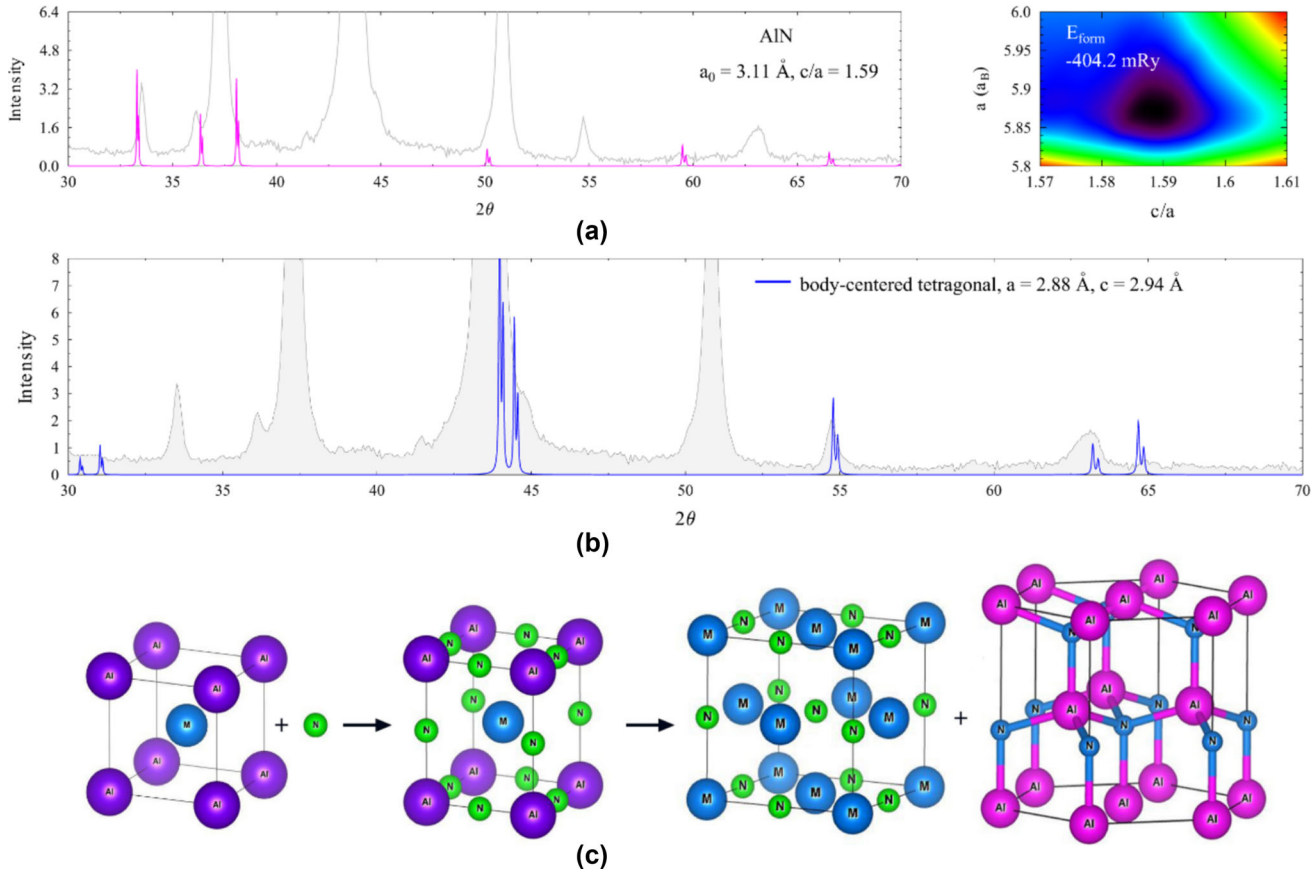

Fig. 16—(*a*) theoretical XRD pattern, lattice parameters, and energy of formation for AlN; (*b*) theoretical XRD pattern and lattice parameters for BCT ($AlCrCoFeNiTi_{0.2}$)N (*c*) Scheme of structural phase transitions path, caused by plasma nitriding. M stands for ($CrCoFeNiTi_{0.2}$) "pseudoatom." Images were rendered using VESTA software Ref. [33].

might consider the BCC → BCT → FCC transformation path (Figure 16(c)), known as the Bain Path,[46,47] which has been reported for Fe and FeCo.[48] Immediately after plasma nitriding, nitrogen occupies the octahedral sites ($\frac{1}{2}$,0,0) in the BCC structure. This distortion leads to an intermediate phase— a body-centered tetragonal structure with a c/a ratio lower than $\sqrt{2}$. The next stage involves the formation of the most common structures of stoichiometric 3d metal nitrides, namely NaCl-type/ZnS-type fcc structures. Based on this description of the Bain path, we calculated theoretical XRD pattern using the experimental lattice constant of the BCC phase (2.89 Å) and scaling the c value to achieve the best convergence between the experiment and calculations. The estimated lattice constant c = 2.94 Å satisfies the condition $c < \sqrt{2}a$.

As previously mentioned, the shift between the calculated and experimental XRD pattern of the NaCl-type ($AlCrCoFeNiTi_{0.2}$)N may be due to the decomposition into simpler nitrides composed of one or two transition metal atoms. These nitrides have different lattice constants compared to ($AlCrCoFeNiTi_{0.2}$)N. Hence, a detailed analysis of these nitrides was conducted, as presented in the Supplementary Information, confirming the presence of (Ti,Cr)N, which is consistent with the EDS and EBSD results.

Notably, our DFT calculations are consistent with thermodynamic studies presented in the literature. The energies of formation found in the literature, sometimes also called heats of formation or enthalpies of formation, of the binary nitrides formed from the metals present in the investigated alloy are presented in Table II.[49–53] In thermodynamics one usually uses $\frac{kJ}{mol}$ units. 1 mRy = 1.306 $\frac{kJ}{mol}$.

Ti, Al, and Cr are the strongest nitride formers and have the lowest heats of formation. The energy required for the formation of the Co and Ni nitrides was close to 0 kJ/mol. This explains the presence of simple AlN and ternary (Ti,Cr)N, which is consistent with the DFT results. According to DFT, TiN has the lowest energy of formation, followed by AlN, CrN, and ($AlCrCoFeNiTi_{0.2}$)N. FeN, which was not observed experimentally, was not formed because it has a higher energy of formation than the created high-entropy nitride.

The rate and amount of diffusion should be considered to explain the presented results fully. It has been previously reported that alloyed elements noticeably compete for the introduced nitrogen atoms to bond with them and form nitrides. In many papers it was observed that only the strongest nitride formers create multiple nitrides in the surface layer during nitriding.[8,15,16,18,19,54] Notably, for low Al concentrations,

Table II. Heat of Formation, ΔH^{for}, of the Binary Nitrides Based on the Constituent Elements of the Present Alloy

Nitrides	TiN	AlN	CrN	FeN	CoN	Ni_3N
$\Delta H^{for}\left[\frac{kJ}{mol}\right]$	− 338	− 318	− 125	− 47	0	+ 0.2

no simple nitride was formed with this component, even though it had the lowest enthalpy of formation.[9,16,54,55] However, it was observed that, for example, in the $Al_{0.3}$CoCrFeNi alloy, elements segregate by the heat of formation, and two areas are formed: one rich in Al–Cr–N and the second rich in Co–Fe–Ni.[15] It has also been reported that the strongest nitride formers diffused onto the surface.[8,18] In our study, Ti diffused to the surface, pushing Al into the depths where AlN and complementary phases were created.

To reduce the competition between nitride formers and enhance the formation of solid solutions, diffusion can be increased by increasing the temperature. In, a[13,14] supersaturated N solid solution was obtained by increasing the nitriding temperature of CoCrFeMnNi to 773 K or higher. Another approach involves increasing the proportion of nitrogen ions during nitriding. It was found in Reference 56 that by the addition of a N_2 flow higher than 14 pct, only a simple NaCl structure could be obtained. Hence, increasing the ratio of N ions in the atmosphere could help prepare a surface made of a single high-entropy nitride without the other phases observed in this work. Mixed hydrogen and nitrogen atmospheres, which are typically used for plasma nitriding, have the lowest nitrogen ion content. However, the flows of argon and nitrogen can be used to obtain much higher amounts of N^+ and N^{2+} during the glow discharge process. These approaches should be carefully investigated in future studies.

V. CONCLUSION

In this study, we performed a detailed analysis of the complex phase transformation of a plasma-nitrided $AlCoCrFeNiTi_{0.2}$ alloy. We investigated its microstructure and mechanical properties using scanning electron microscopy-energy dispersive X-ray spectroscopy, EBSD, XRD, and numerical analysis based on DFT simulations. Plasma nitriding led to the formation of a coating with a sophisticated microstructure. At the top, a highly dislocated nanocrystalline layer, rich in titanium high-entropy nitride, was observed. It exhibited higher hardness and a significantly lower coefficient of friction compared to the virgin alloy. Below this layer, a porous (Ti, Cr)N layer was formed. Deeper layers revealed a mixture of AlN, (Ti, Cr)N, and NaCl-type $(AlCrCoFeNiTi_{0.2})N$. Finally, at the bottom of the investigated cross-section, AlCoCrFeNi with a small amount of nitrogen interstitials was observed.

However, plasma nitriding caused high porosity, which resulted in lower mechanical properties in certain areas. Nonetheless, carefully chosen spots with minimal or no porosity exhibited a hardness of up to approximately 9 GPa, significantly greater than the maximal measured hardness of the virgin sample (7 GPa). This process also prevented brittle fracture during plastic deformation, as measured by pillar compression, and reduced friction. The coefficient of friction was almost 10 times smaller.

In summary, detailed experimental and numerical approaches enabled a precise understanding of the obtained results and brought us closer to understanding the mechanisms governing the nitriding process of dual-phase HEAs.

ACKNOWLEDGMENTS

The authors acknowledge the support of the National Science Centre in Poland through Grant 2021/43/B/ST8/02895.

CONFLICT OF INTEREST

On behalf of all authors, the corresponding author states that there is no conflict of interest.

SUPPLEMENTARY INFORMATION

The online version contains supplementary material available at https://doi.org/10.1007/s11661-025-07752-1.

REFERENCES

1. Y. Zhang: High-Entropy Materials Advances and Applications, 1st ed. CRC Press, Boca Raton, 2024.
2. S. Akrami, P. Edalati, M. Fuji, K. Edalati: High-entropy ceramics: review of principles, production and applications. In Materials Science and Engineering R: Reports. Elsevier Ltd., vol. 146, 2021. https://doi.org/10.1016/j.mser.2021.100644..
3. H. Xiang, Y. Xing, Dai, F. Zhi, H. Wang, L. Su, L. Miao, G. Zhang, Y. Wang, X. Qi, L. Yao, H. Wang, B. Zhao, J. Li, Y. Zhou: High-entropy ceramics: Present status, challenges, and a look forward. In Journal of Advanced Ceramics, vol. 10, issue 3, pp. 385–441, 2021, Tsinghua University. https://doi.org/10.1007/s40145-021-0477-y.
4. R. Chen, Z. Cai, J. Pu, Z. Lu, S. Chen, S. Zheng, and C. Zeng: J. Alloys Compd., 2020, Vol. 827, p. 153836. https://doi.org/10.1016/j.jallcom.2020.153836.
5. S. Alvi, M. Milczarek, D.M. Jarzabek, D. Hedman, M.G. Kohan, N. Levintant-Zayonts, A. Vomiero, and F. Akhtar: Adv. Eng. Mater. (n.d.). vol. 24, no. 9, p. 2101626 https://doi.org/10.1002/adem.202101626.
6. E. Lewin: J. Appl. Phys., 2020, vol.127. https://doi.org/10.1063/1.5144154.
7. K. Johansson, L. Riekehr, S. Fritze, and E. Lewin: *Surf. Coat. Technol.*, 2018, vol. 349, pp. 529–39. https://doi.org/10.1016/j.surfcoat.2018.06.030.
8. Y. Wang, Y. Yang, H. Yang, M. Zhang, and J. Qiao: *J. Alloys Compd.*, 2017, vol. 725, pp. 365–72. https://doi.org/10.1016/j.jallcom.2017.07.132.
9. W.-Y. Tang, M.-H. Chuang, H.-Y. Chen, and J.-W. Yeh: *Surf. Coat. Technol.*, 2010, vol. 204, pp. 3118–124. https://doi.org/10.1016/j.surfcoat.2010.02.045.
10. Y. Zhang, High-Entropy Materials, Springer, Singapore, 2019.
11. H. Xiang, Y. Xing, F. Dai, H. Wang, L. Su, L. Miao, G. Zhang, Y. Wang, X. Qi, L. Yao, H. Wang, B. Zhao, J. Li, and Y. Zhou: *J. Adv. Ceram.*, 2021, vol. 10, pp. 385–441. https://doi.org/10.1007/s40145-021-0477-y.
12. S. Akrami, P. Edalati, M. Fuji, K: Mater. Sci. Eng. R., 2021, vol. 146. https://doi.org/10.1016/j.mser.2021.100644.
13. T. Karimoto and A. Nishimoto: *Metals*, 2020, vol. 10, pp. 1–2. https://doi.org/10.3390/met10060761.
14. A. Nishimoto, T. Fukube, and T. Maruyama: *Surf. Coat. Technol.*, 2019, vol. 376, pp. 52–58. https://doi.org/10.1016/j.surfcoat.2018.06.088.
15. W. Wang, S. Song, K.M. Reddy, W. Li, P. Liu, and X. Wang: Mater. Lett. 2019, vol. 255. https://doi.org/10.1016/j.matlet.2019.126566.
16. J. Hou, W. Song, L. Lan, and J. Qiao: J. Mater. Sci. Technol. 48, 2020, vol. 140–45. https://doi.org/10.1016/j.jmst.2020.01.057.
17. L.W. Lan, H.J. Yang, R.P. Guo, X.J. Wang, M. Zhang, P.K. Liaw, and J.W. Qiao: *Mater. Chem. Phys.*, 2021, vol. 270, p. 124800. https://doi.org/10.1016/j.matchemphys.2021.124800.
18. Y. Wang, Y. Yang, H. Yang, M. Zhang, S. Ma, and J. Qiao: *Mater. Chem. Phys.*, 2018, vol. 210, pp. 233–39. https://doi.org/10.1016/j.matchemphys.2017.05.029.
19. Z. Cai, Z. Wang, Y. Hong, B. Lu, J. Liu, Y. Li, and J. Pu: *Tribol. Int.*, 2021, vol. 163, p. 107195. https://doi.org/10.1016/j.triboint.2021.107195.
20. Y. Kuan Zhou, J. Jie Kang, J. Zhang, S. Zhu, Z. Qiang Fu, L. Na Zhu, and D. Shun She: Intermetallics (Barking), 2022, vol. 151, p.107709. https://doi.org/10.1016/j.intermet.2022.107709.
21. P. Jenczyk, D.M. Jarzabek, Z. Lu, E. Gadalinska, N. Levintant-Zayonts, and Y. Zhang: Mater Des, 2022, vol. 216, p. 1105-68.https://doi.org/10.1016/j.matdes.2022.110568.
22. B.D. Cullity: *Elements of X-ray Diffcation*, Addison-Wesley, Boston, 1978.
23. W.C. Oliver and G.M. Pharr: *J. Mater. Res.*, 2004, vol. 19, pp. 3–20. https://doi.org/10.1557/jmr.2004.19.1.3.
24. J.E. Sader, I. Larson, P. Mulvaney, and L.R. White: *Rev. Sci. Instrum.*, 1995, vol. 66, pp. 3789–98. https://doi.org/10.1063/1.1145439.
25. C. Dziekoński, W. Dera, and D.M. Jarząbek: *Ultramicroscopy*, 2017, vol. 182, pp. 1–9. https://doi.org/10.1016/j.ultramic.2017.06.012.
26. H. Grzywacz, M. Milczarek, P. Jenczyk, W. Dera, M. Michalowski, and D.M. Jarzabek: *Measurement*, 2021, vol. 168, p. 108267. https://doi.org/10.1016/j.measurement.2020.108267.
27. P. Soven: Phys. Rev., 1967, vol. 156, p. 809. https://doi.org/10.1103/PhysRev.156.809.
28. H. Ebert, D. Koedderitzsch, andJ. Minar: Rep. Prog. Phys., 2011, vol. 74. https://doi.org/10.1088/0034-4885/74/9/096501.
29. H Ebert et al., The Munich SPR-KKR package, version 8.6, https://www.ebert.cup.uni-muenchen.de/sprkkr. (n.d.).
30. S.H. Vosko, L. Wilk, and M. Nusair: *Can. J. Phys.*, 1980, vol. 58, pp. 1200–11. https://doi.org/10.1139/p80-159.
31. P. Lloyd, Proc. Phys. Soc., 1967, vol. 90, p. 207. https://doi.org/10.1088/0370-1328/90/1/323.
32. F. Birch: *Phys. Rev.*, 1947, vol. 71, pp. 809–24. https://doi.org/10.1103/PhysRev.71.809.
33. K. Momma and F. Izumi: *J. Appl. Crystallogr.*, 2011, vol. 44, pp. 1272–76. https://doi.org/10.1107/S0021889811038970.
34. E. Menendez, C. Templier, P. Garcia-Ramirez, J. Santiso, A. Vantomme, K. Temst, and J. Nogues: *ACS Appl. Mater. Interfaces*, 2013, vol. 5, pp. 10118–26. https://doi.org/10.1021/am402773w.
35. X. Tao, A. Matthews, and A. Leyland: *Metall. Mater. Trans. A Phys. Metall. Mater. Sci.*, 2020, vol. 51, pp. 436–47. https://doi.org/10.1007/s11661-019-05526-0.
36. K.H. Lee, C.H. Park, Y.S. Yoon, and J.J. Lee: *Thin Solid Films*, 2001, vol. 385, pp. 167–73. https://doi.org/10.1016/S0040-6090(00)01911-8.
37. B. Bhushan and A. V Kulkarni: Thin Solid Films, 1996, vol. 278, pp. 49–56. https://doi.org/10.1016/0040-6090(95)08138-0.
38. P. Qiao, J. Xie, Y. Jiang, P. Tang, B. Liang, Y. Lu, and J. Gong: Coatings, 2022, vol. 12. https://doi.org/10.3390/coatings12121917.
39. C.C. Silva, J.P. Farias, H.C. Miranda, R.F. Guimarães, J.W.A. Menezes, and M.A.M. Neto: *Mater Charact*, 2008, vol. 59, pp. 528–33. https://doi.org/10.1016/j.matchar.2007.03.011.
40. M. Vach, T. Kuníková, M. Dománková, P. Ševc, Ľ Čaplovič, P. Gogola, and J. Janovec: *Mater Charact*, 2008, vol. 59, pp. 1792–98. https://doi.org/10.1016/j.matchar.2008.04.009.
41. D. You, G. Yang, Y.H. Choa, and J.K. Kim: Mater. Sci. Eng.. A, 2022, vol. 831. https://doi.org/10.1016/j.msea.2021.142039.
42. T. Huhne, C. Zecha, H. Ebert, P.H. Dederichs, and R. Zeller: *Phys. Rev. B*, 1998, vol. 58, pp. 10236–47. https://doi.org/10.1103/PhysRevB.58.10236.
43. K. Jasiewicz, S. Kaprzyk, and J. Tobola: Acta Phys. Pol. A, 2018, vol. 133, pp. 511–13. https://doi.org/10.12693/APhysPolA.133.511.
44. K. Jasiewicz, J. Cieslak, S. Kaprzyk, and J. Tobola: *J. Alloys Compd.*, 2015, vol. 648, pp. 307–12. https://doi.org/10.1016/j.jallcom.2015.06.260.
45. S. Strite and H. Morkoc: *J. Vac. Sci. Technol. B*, 1992, vol. 10, pp. 1237–66. https://doi.org/10.1116/1.585897.
46. B. Roldan Cuenya, M. Doi, S.L.R. Courths, W. Keune, Observation of the fcc-to-bcc Bain transformation in epitaxial Fe ultrathin ®lms on Cu 3 Au(0 0 1), n.d. www.elsevier.com/locate/susc.
47. J.S. Bowles and C.M. Wayman: *Metallurgical Transactions*, 1972, vol. 3, pp. 1113–21. https://doi.org/10.1007/BF02642442.
48. T. Burkert, L. Nordström, O. Eriksson, and O. Heinonen, Phys Rev Lett, 2004, Vol. 93. https://doi.org/10.1103/PhysRevLett.93.027203.
49. A.R. Miedema, On the Heat of Formation of Solid Alloys. II, Elsevier Sequoia S.A, 1976.
50. A.K. Niessen and F.R. De Boer: *J. Less-Common Met.*, 1981, vol. 82, pp. 75–80. https://doi.org/10.1016/0022-5088(81)90200-9.
51. F.R. de Boer, W.C.M. Mattens, R. Boom, A.R. Miedema, A.K. Niessen, Cohesion in Metals, Cohesion and Structure, 1988.
52. M.W. Chase Jr.: *NIST-JANAF thermochemical tables, monograph 9*, American Chemical Society, Washington DC, 1998.
53. E. Lewin: *J. Appl. Phys.*, 2020, https://doi.org/10.1063/1.5144154.
54. W.Y. Tang and J.W. Yeh: *Metall. Mater. Trans. A Phys. Metall. Mater. Sci.*, 2009, vol. 40, pp. 1479–86. https://doi.org/10.1007/s11661-009-9821-5.
55. W.Y. Tang, M.H. Chuang, S.J. Lin, and J.W. Yeh: *Metall. Mater. Trans. A Phys. Metall. Mater. Sci.*, 2012, vol. 43, pp. 2390–2400. https://doi.org/10.1007/s11661-012-1108-6.

56. C.H. Lai, S.J. Lin, J.W. Yeh, and S.Y. Chang: *Surf. Coat. Technol.*, 2006, vol. 201, pp. 3275–80. https://doi.org/10.1016/j.surfcoat.2006.06.048.